biosensors

MDPI

Communication

High Performance of a Metal Layer-Assisted Guided-Mode Resonance Biosensor Modulated by Double-Grating

Chengrui Zhang †, Yi Zhou †, Lan Mi, Jiong Ma, Xiang Wu and Yiyan Fei *

Department of Optical Science and Engineering, Shanghai Engineering Research Center of Ultra-Precision Optical Manufacturing, Key Laboratory of Micro and Nano Photonic Structures (Ministry of Education), School of Information Science and Technology, Fudan University, Shanghai 200433, China; 19210720089@fudan.edu.cn (C.Z.); 18110720008@fudan.edu.cn (Y.Z.); lanmi@fudan.edu.cn (L.M.); jiongma@fudan.edu.cn (J.M.); wuxiang@fudan.edu.cn (X.W.)

* Correspondence: fyy@fudan.edu.cn

† These authors contributed equally to the manuscript.

Abstract: Guided-mode resonance (GMR) sensors are widely used as biosensors with the advantages of simple structure, easy detection schemes, high efficiency, and narrow linewidth. However, their applications are limited by their relatively low sensitivity (<200 nm/RIU) and in turn low figure of merit (FOM, <100 1/RIU). Many efforts have been made to enhance the sensitivity or FOM, separately. To enhance the sensitivity and FOM simultaneously for more sensitive sensing, we proposed a metal layer-assisted double-grating (MADG) structure with the evanescent field extending to the sensing region enabled by the metal reflector layer underneath the double-grating. The influence of structural parameters was systematically investigated. Bulk sensitivity of 550.0 nm/RIU and FOM of 1571.4 1/RIU were obtained after numerical optimization. Compared with a single-grating structure, the surface sensitivity of the double-grating structure for protein adsorption increases by a factor of 2.4 times. The as-proposed MADG has a great potential to be a biosensor with high sensitivity and high accuracy.

Keywords: sensors; guided-mode resonance; figure of merit; grating

Citation: Zhang, C.; Zhou, Y.; Mi, L.; Ma, J.; Wu, X.; Fei, Y. High Performance of a Metal Layer-Assisted Guided-Mode Resonance Biosensor Modulated by Double-Grating. *Biosensors* **2021**, *11*, 221. https://doi.org/10.3390/bios11070221

Received: 9 June 2021
Accepted: 1 July 2021
Published: 3 July 2021

1. Introduction

The advanced analytical biosensors are widely used as molecules detection and diagnostic tools, which are able to probe the interactions between chemical and biological molecules with high sensitivity and have found extensive applications in disease diagnosis, drug development, environmental pollution monitoring, and food safety detection [1–3]. The emergence of nanotechnology and nanofabrication has given rise to a variety of label-free biosensor technologies, such as cladding-mode resonance biosensors based on short- or long-period fiber gratings [4], Mach–Zehnder interferometer biosensors [5,6], surface plasmon resonance (SPR) biosensors [7–9], and guided mode resonance (GMR) biosensors [10–15].

GMR refers to the resonance between the incident light modulated by the grating and the conduction mode of the waveguide, and the GMR effect is widely used in the sensing field due to the advantages of simple structure, easy detection schemes, high efficiency, and narrow linewidth [12]. However, GMR sensors typically have relatively low sensitivity (<200 nm/RIU) and a small figure of merit (FOM, <100 1/RIU), which is defined as the sensitivity of the sensor divided by the full width at half maximum (FWHM) of the resonance (Sensitivity/FWHM) [16–20]. Biosensors with large sensitivity and FOM are more desirable since a large signal noise ratio is achievable for accurate detection of small signals during biosensing [21–23]. Many research groups have proposed several ways to improve the sensitivity of GMR sensors. Lu et al. proposed a compound waveguide grating biosensor via a modulated wave vector to enhance the sensitivity up to 345 nm/RIU, which is two times higher in magnitude than the normal case [18]. Wan et al. designed an ultralow refractive

index porous silicon dioxide structure to make the resonance mode reside mainly in the sensing medium, which resulted in a sensitivity of up to 546 nm/RIU. In addition, metal structures are also used to improve the sensitivity of the sensor [24]. Lin et al. utilized a metal layer-assisted guided mode resonance (MaGMR) sensor to make the evanescent wave distribute asymmetrically in the waveguide layer which resulted in distribution of more electric field intensity in the analytes. The sensitivity of such a structure is 338.5 nm/RIU, increased by a factor of 1.5 over conventional structures [17]. Wang et al. proposed a hybrid guided-mode resonance/surface plasmon resonance structure to increase sensitivity to 1087 nm/RIU with a resonance wavelength of 1796.1 nm [25].

These reports demonstrated obvious sensitivity enhancement. However, the resonant linewidth also broadened (>10 nm) and the resultant FOM values were still small (~20 1/RIU). Some research groups also devoted their attention to improving the FOM values through narrowing the resonance linewidth without special efforts to increase sensitivity [13,15,26]. Lan et al. proposed a all-dielectric nano-silt arrayguided mode resonance sensor, and ultra-high FOM (~12,000 1/RIU) values were achieved with sensitivity in the range of 240 nm/RIU [26].

In this work, we proposed a GMR sensor with simultaneous enhancement of sensitivity and FOM. We explored a metal layer-assisted double-grating (MADG) structure-based GMR which consists of a substrate, a metal reflector and a double dielectric grating with two ridges in a period. With numerical simulation, we demonstrated that the bulk sensitivity of 550.0 nm/RIU and FOM of 1571.4 1/RIU can be achieved simultaneously. The proposed MADG-based GMR sensor has great potential in biosensing applications which require high sensitivity and a low detection limit.

2. Optimization of MADG Structure

2.1. MADG Structure

The proposed MADG structure that excites GMR is shown in Figure 1. On top of the SiO_2 substrate, there is a metal reflector layer (Au) which is covered with a dielectric layer (HfO_2, n_g = 1.95) [27]. The metal reflector layer thickness is H_m. The dielectric layer is designed to be a double grating which is composed of two ridges with identical width in a period. With a grating period of Λ and fill factors f and f_i, the width of each ridge is $f \times \Lambda$, the interval between two ridges is $f_i \times \Lambda$, and the interval between two periods is $(1 - 2f - f_i) \times \Lambda$. The depth of the grating is H_g. The refractive index of the top medium surrounded the MADG structure is n_a. The resonant features and electric field distribution of the MADG-based GMR structure were simulated with COMSOL Multiphysics 5.2a (COMSOL Inc., Stockholm, Sweden) [28].

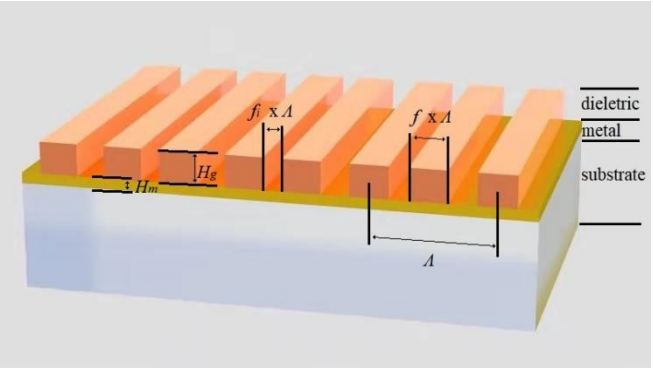

Figure 1. Configuration of MADG structure.

2.2. Influence of f_i on MADG Based GMR Sensor Performance

With Λ being set at 500 nm, H_g at 300 nm, H_m at 100 nm and fill factor f at 0.25, we studied how the fill factor f_i affected the MADG-based GMR's performance. As shown in Figure 2a, the resonance wavelength is in the range of visible light, which demonstrates a

red shift, with f_i increasing from 0 to 0.225. When f_i is close to 0.25, the resonance disappears. With f_i increasing from 0.275 to 0.5, there are strong resonances again with features the same as resonances at $0.5 - f_i$.

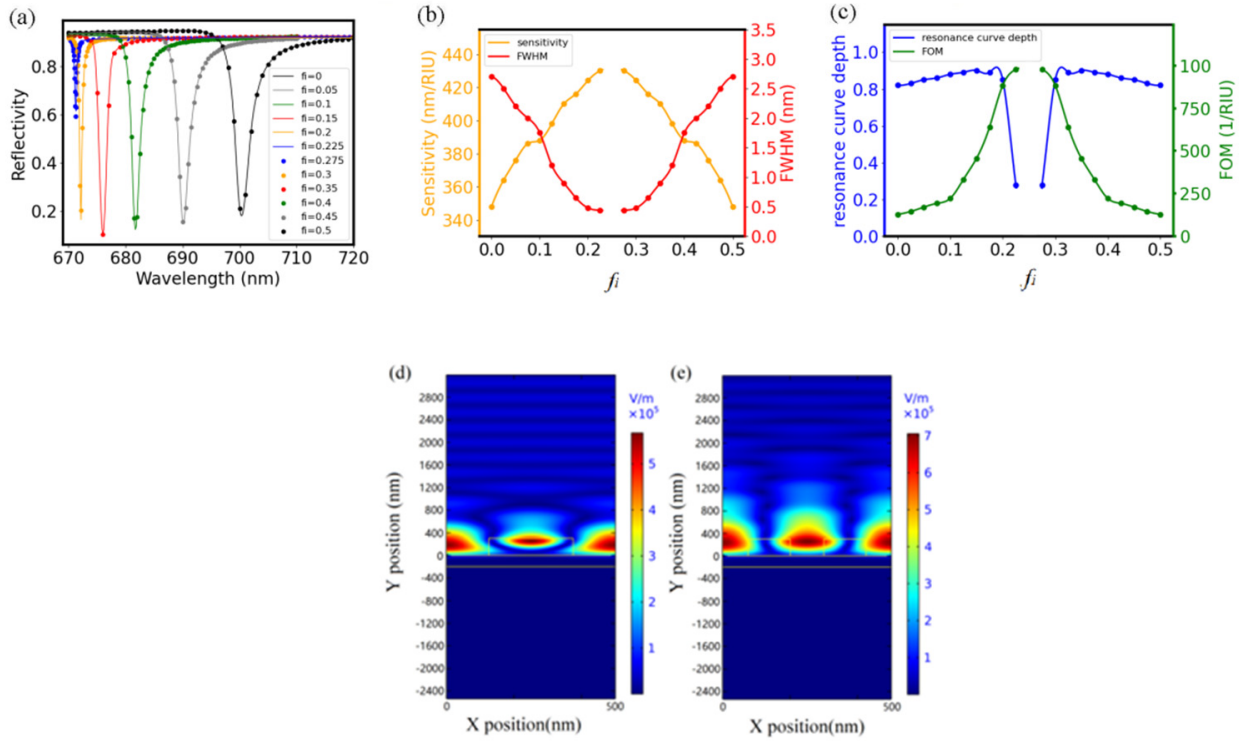

Figure 2. (**a**) Reflection spectrum of MADG based GMR sensor with f_i ranging from 0 to 0.5 for the normal incident TE polarized light (electric field perpendicular to the plane of incidence light with normal direction of interface). (**b**) Dependence of sensitivity and FWHM of MADG based GMR on f_i. (**c**) Dependence of FOM and resonance curve depth on *fi*. (**d**) Electric field distribution of GMR with $f_i = 0$ and with (**e**) $f_i = 0.2$. For simulation, Λ was set at 500 nm, H_g at 300 nm, H_m at 100 nm, and fill factor f at 0.25.

Figure 2b shows that the sensitivity of the GMR sensor increases and FWHM decreases monotonically with f_i less than 0.25. In addition, the sensitivity decreases and FWHM increases monotonically with f_i larger than 0.25. The sensitivity and FWHM are not shown for $f_i = 0.25$ where resonance disappears. As demonstrated in Figure 2c, the FOM of the MADG-based GMR sensor maximizes with f_i close to 0.25, similar to the behavior of the sensitivity.

Figure 2d,e show the electric field distribution of the MADG-based GMR structure with $f_i = 0$ and $f_i = 0.2$, respectively. Due to the metal layer underneath the grating, no electric field distributes in the substrate and the evanescent diffraction field distributes mostly in the top medium for sensing. Around the grating ridge, most of the electric field is located inside the ridge with $f_i = 0$, while it is mostly distributes in the top medium between two ridges with $f_i = 0.2$. In addition, the penetration depth of the evanescent diffraction field is deeper with $f_i = 0.2$. The distribution of the electric field in the top medium and the deep penetration depth with $f_i = 0.2$ demonstrate that the MADG-based GMR sensor provides more evanescent energy for sensing, which may be responsible for the improvement in the sensitivity with the double grating structure [29]. The larger overlap area between analytes and evanescent diffraction field provided by the MADG structure has the potential to enhance the sensitivity of the techniques taking advantage of evanescent field, such as the plasmon-enhanced fluorescence method for the detection of molecules of various sizes [30,31].

The change in FWHM with f_i can be attributed to the coupling changes between evanescent diffraction fields and the leaky guided modes. The permittivity of the periodic grating can be expanded into Fourier series [32],

$$\varepsilon = \sum_n \varepsilon_n exp\left(i\frac{2n\pi x}{\Lambda}\right) \quad (1)$$

where the Fourier harmonic coefficients ε_n can be expressed as,

$$\varepsilon_0 = 2fn_g^2 + (1-2f)n_a^2 \quad (2)$$

$$\varepsilon_n = (n_g^2 - n_a^2)\frac{sin[n\pi(1-2f-f_i)] - sin(n\pi f_i)}{n\pi}, \ (n = \pm 1, \pm 2, \ldots \pm N \ldots) \quad (3)$$

According to the rigorous coupled-wave theory [33], the Fourier harmonic coefficients ε_n regulate the interaction among evanescent diffraction fields and the leaky guided modes [30]. Since the MADG-based GMR sensor excites leaky guided modes through the first evanescent diffracted order of the grating, the coupling between the evanescent diffraction fields and the leaky guided modes is mainly determined by ε_1. Equation (3) shows that $|\varepsilon_1|$ decreases to zero when f_i changes from 0 to 0.25 and $|\varepsilon_1|$ increases from zero with f_i changing from 0.25 to 0.5. Smaller $|\varepsilon_1|$ signifies poorer coupling, causing decreased spectrum linewidth [32], which may explain behaviors of FWHM.

One more feature in Figure 2a is the depth of the resonance curve, which is defined as reflectivity at the inflection point minus the reflectivity at the resonance point. Figure 2c shows that the resonance curve depths are close to 0.8 with f_i less than 0.2 and decrease sharply to around 0.1 with f_i changing from 0.2 to 0.25. Since resonance signals with larger depth have better noise tolerating capability for better sensing performance, f_i = 0.2 is used in the following simulations with which large sensitivity, large FOM and large resonance curve depth are all achievable.

2.3. Influence of H_m on MADG Based GMR Sensor Performance

With Λ at 500 nm, H_g at 300 nm, f at 0.25, and f_i at 0.2, we studied the influences of the metal reflector layer underneath the double grating on performance of GMR sensor. As shown in Figure 3a,b, the sensitivity increases and the FWHM decreases with H_m, which results in FOM increasing with H_m. The FOM almost levels off when H_m is larger than 100 nm, meaning that H_m = 100 nm is used in the following simulations. In addition, the resonance curve depth is close to 0.9 with H_m = 100 nm which provides good noise tolerating capability.

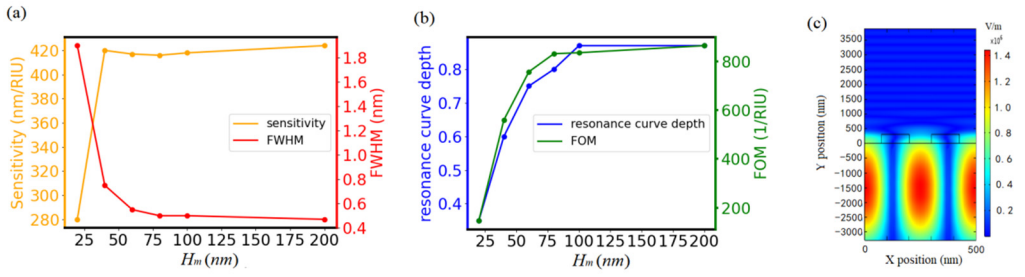

Figure 3. (**a**) Dependence of sensitivity and FWHM on H_m. (**b**) Dependence of FOM and resonance curve depth on H_m. (**c**) Electric field distribution of GMR with no metal reflector layer. For simulation, Λ was set at 500 nm, H_g at 300 nm, fill factor f at 0.25, and f_i at 0.2.

To understand the increase in sensitivity with H_m, Figure 3c shows the electric field distribution of GMR without the metal reflector layer. Compared with the electric field distribution with the metal reflector layer shown in Figure 2e, most of the electric field distributes in the substrate layer rather than in the analytes when there is no metal reflector

layer. The increase in sensitivity from 15 nm/RIU with H_m = 0 nm to 420 nm/RIU with H_m = 100 nm could be due to the asymmetrical evanescent diffraction field wave distribution in the waveguide layer and the distribution of more electric field intensity in the analytes [19].

2.4. Influence of Λ and H_g on MADG Based GMR Sensor Performance

Figure 4a,b show the dependence of GMR performance on Λ with Hm at 100 nm, f at 0.25, and f_i at 0.2. To obtain resonance curves under phase matching conditions with Λ ranging from 480 to 660 nm, Hg was set at 380 nm. It is clear that a large Λ provides high sensitivity and small FWHM, which is similar to the previous studies [34,35]. Even though both sensitivity and FOM monotonically increase with Λ within the range of simulations, resonance curve depths drop dramatically with Λ at 660 nm. In this case, Λ = 640 nm is used for following simulations. In addition, the resonant wavelength at Λ = 640 nm is 858.2 nm, which makes the as-designed sensor a promising candidate for applications with high sensitivity and relatively low absorption in water.

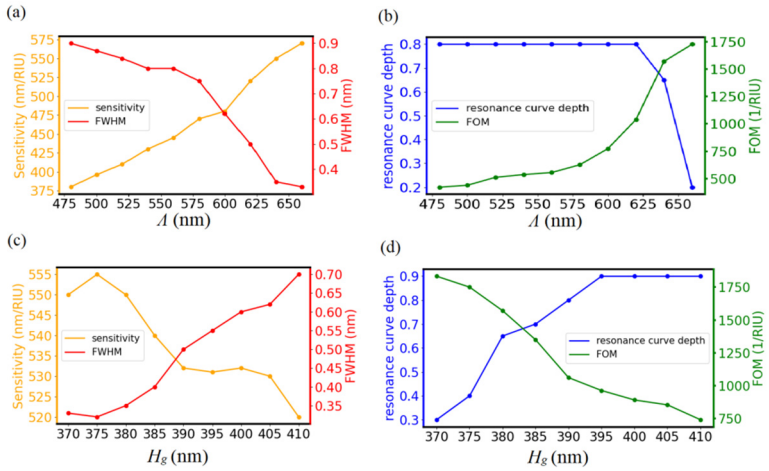

Figure 4. (**a**) Dependence of sensitivity and FWHM (**b**) resonance curve depth and FOM on Λ with H_g at 380 nm, H_m t at 100 nm, f at 0.25, and f_i at 0.2. (**c**) Dependence of sensitivity and FWHM (**d**) resonance curve depth and FOM on H_g with Λ at 640 nm, H_m at 100 nm, f at 0.25, and f_i at 0.2.

Figure 4c,d show the dependence of GMR performance on grating H_g with Λ at 640 nm, H_m at 100 nm, f at 0.25, and f_i at 0.2. In order to satisfy the phase matching condition with Λ at 640 nm, H_g varies from 370 to 410 nm. Both sensitivity and FOM decrease with H_g and maximal FOM is located at 370 nm, at which the resonance curve depth is only 0.3. To obtain large sensitivity and FOM with acceptable resonance curve depth, H_g = 380 nm was used for following simulations.

2.5. Bulk and Surface Sensitivity

With Λ at 640 nm, H_g at 380 nm, H_m at 100 nm, f at 0.25, and f_i at 0.2, the MADG-based GMR sensor was immersed in liquids with increasing refractive indices. Figure 5a,b show that the resonance wavelength increases linearly with refractive index and the slope (i.e., bulk sensitivity) is 550.0 nm/RIU. With FWHM being 0.35 nm, FOM is calculated to be 1571.4 1/RIU. Comparing with other GMR sensors, the MADG-based GMR sensor provides both high sensitivity and a large FOM, as shown in Table 1.

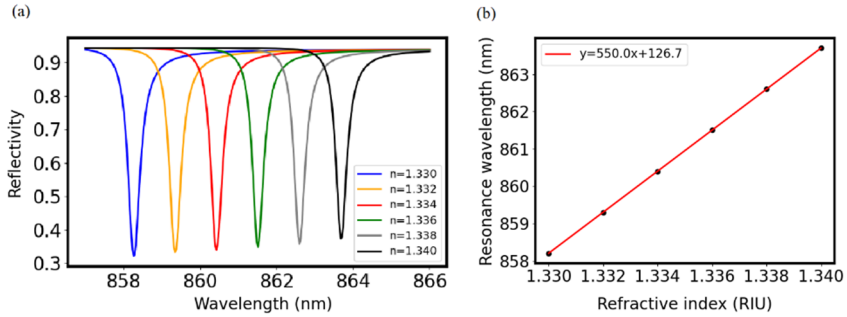

Figure 5. (**a**) Reflection spectra of the MADG-based GMR sensor immersed in liquids with increasing refractive indices. (**b**) Resonance wavelength of the MADG-based GMR sensor changes as a function of the liquid refractive index. For simulation, Λ was set at 640 nm, H_g at 380 nm, H_m at 100 nm, f at 0.25, and f_i at 0.2.

Table 1. Sensitivity, FOM, and resonance wavelength of some GMR sensors.

GMR Sensors	Sensitivity (nm/RIU)	FOM (1/RIU)	Wavelength (nm)	Reference
MADG based GMR device	550.0	1571	858.2	This work
One-dimensional all-dielectric nano-slit array	240	12,000	819	[26]
Hybird GMR/SPR sensor	1087	23	1796.1	[25]
Compound waveguide grating	345	17.3	1580	[18]
Ultralow RI substrate GMR	546	~273	~784	[24]

We then investigated the surface sensitivity with the protein sample adsorbing on the MADG-based GMR sensor. For simulation, we assumed a refractive index of 1.5 [36] and the protein thickness increasing from 0 nm to 20 nm to calculate the surface sensitivity [37]. Figure 6b shows the resonant wavelength of GMR as a function of the protein thickness. The sensitivity of MADG with double grating is 0.415 nm/nm, which is 2.4 times of that of metal assist single grating and 5.5 times of that of double grating without metal layer.

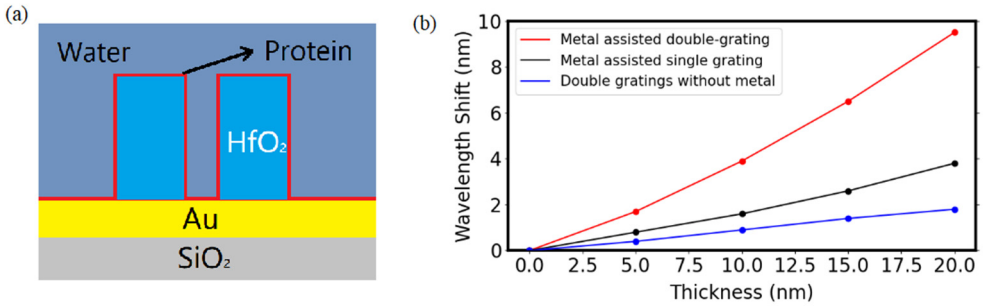

Figure 6. (**a**) Protein adsorption on the MADG-based GMR sensor. (**b**) The shift of resonant wavelength as a function of the protein thickness on GMR sensor. Λ was set at 640 nm, H_g at 380 nm, H_m at 100 nm, f at 0.25, and f_i at 0.2.

3. Results

In summary, a metal layer-assisted guided mode resonance biosensor modulated by a double grating structure was designed to achieve both high sensitivity and high FOM for optical biosensing. The sensitivity is increased by the metal reflector under the double grating layer, which causes asymmetrical electric field distribution and leads to longer penetration depth and larger overlap area between the analytes and the evanescent diffraction field. The spectral linewidth is optimized through double grating by modulating coupling between the evanescent diffraction fields and the leaky guided modes. With optimization,

the MADG-based GMR sensor is able to provide bulk sensitivity of 550.0 nm/RIU and FOM of 1571.4 1/RIU, which shows great potential for sensitive label-free biosensing.

Author Contributions: Conceptualization, X.W.; Data curation, C.Z. and Y.Z.; Formal analysis, C.Z. and Y.Z.; Funding acquisition, X.W. and Y.F.; Investigation, C.Z.; Methodology, C.Z. and Y.Z.; Project administration, Y.F.; Resources, Y.F.; Supervision, X.W. and Y.F.; Writing—original draft, C.Z.; Writing—review and editing, L.M., J.M. and Y.F. All authors have read and agreed to the published version of the manuscript.

Funding: This work was financially supported by Shanghai Natural Science Foundation (Grant No. 20ZR1403700), Fudan University-CIOMP Joint Fund (Grant No. FC2020-004), National Natural Science Foundation of China (Grant No. 82030106), Science and Technology Commission of Shanghai Municipality (Grant No. 20JC1410900), and Shanghai Natural Science Foundation (Grant No. 20ZR1405100).

Institutional Review Board Statement: Not applicable.

Informed Consent Statement: Not applicable.

Data Availability Statement: Not applicable.

Conflicts of Interest: The authors declare no conflict of interest.

References

1. Babuin, L.; Jaffe, A.S. Troponin: The biomarker of choice for the detection of cardiac injury. *Can. Med. Assoc. J.* **2005**, *173*, 1191–1202. [CrossRef]
2. Cooper, M.A. Label-free screening of bio-molecular interactions. *Anal. Bioanal. Chem.* **2003**, *377*, 834–842. [CrossRef]
3. Esteller, M.; Herman, J.G. Cancer as an epigenetic disease: DNA methylation and chromatin alterations in human tumours. *J. Pathol.* **2001**, *196*, 1–7. [CrossRef] [PubMed]
4. Yang, F.; Chang, T.L.; Liu, T.; Wu, D.; Du, H.; Liang, J.; Tian, F. Label-free detection of Staphylococcus aureus bacteria using long-period fiber gratings with functional polyelectrolyte coatings. *Biosens. Bioelectron.* **2019**, *133*, 147–153. [CrossRef]
5. Schmid, J.H.; Sinclair, W.; García, J.; Janz, S.; Lapointe, J.; Poitras, D.; Li, Y.; Mischki, T.; Lopinski, G.; Cheben, P.; et al. Silicon-on-insulator guided mode resonant grating for evanescent field molecular sensing. *Opt. Express* **2009**, *17*, 18371–18380. [CrossRef]
6. Xiao, G.; Zhu, Q.; Shen, Y.; Li, K.; Liu, M.; Zhuang, Q.; Jin, C. A tunable submicro-optofluidic polymer filter based on guided-mode resonance. *Nanoscale* **2015**, *7*, 3429–3434. [CrossRef]
7. Cetin, A.E.; Etezadi, D.; Galarreta, B.; Busson, M.P.; Eksioglu, Y.; Altug, H. Plasmonic Nanohole Arrays on a Robust Hybrid Substrate for Highly Sensitive Label-Free Biosensing. *ACS Photonics* **2015**, *2*, 1167–1174. [CrossRef]
8. Fernández, F.; Hegnerová, K.; Piliarik, M.; Sanchez-Baeza, F.; Homola, J.; Marco, M.-P. A label-free and portable multichannel surface plasmon resonance immunosensor for on site analysis of antibiotics in milk samples. *Biosens. Bioelectron.* **2010**, *26*, 1231–1238. [CrossRef]
9. Homola, J.; Yee, S.S.; Gauglitz, G. Surface plasmon resonance sensors: Review. *Sens. Actuators B Chem.* **1999**, *54*, 3–15. [CrossRef]
10. El Beheiry, M.; Liu, V.; Fan, S.; Levi, O. Sensitivity enhancement in photonic crystal slab biosensors. *Opt. Express* **2010**, *18*, 22702–22714. [CrossRef] [PubMed]
11. Choi, C.J.; Block, I.D.; Bole, B.; Dralle, D.; Cunningham, B.T. Label-Free Photonic Crystal Biosensor Integrated Microfluidic Chip for Determination of Kinetic Reaction Rate Constants. *IEEE Sens. J.* **2009**, *9*, 1697–1704. [CrossRef]
12. Cunningham, B.T.; Zhang, M.; Zhuo, Y.; Kwon, L.; Race, C. Recent Advances in Biosensing with Photonic Crystal Surfaces: A Review. *IEEE Sens. J.* **2016**, *16*, 3349–3366. [CrossRef] [PubMed]
13. Zhou, Y.; Li, X.; Li, S.; Guo, Z.; Zeng, P.; He, J.; Wang, D.; Zhang, R.; Lu, M.; Zhang, S. Symmetric guided-mode resonance sensors in aqueous media with ultrahigh figure of merit. *Opt. Express* **2019**, *27*, 34788–34802. [CrossRef] [PubMed]
14. Zhou, Y.; Guo, Z.; Zhou, W.; Li, S.; Liu, Z.; Zhao, X.; Wu, X. High-Q guided mode resonance sensors based on shallow sub-wavelength grating structures. *Nanotechnology* **2020**, *31*, 325501. [CrossRef]
15. Zhou, Y.; Wang, B.; Guo, Z.; Wu, X. Guided Mode Resonance Sensors with Optimized Figure of Merit. *Nanomaterials* **2019**, *9*, 837. [CrossRef]
16. Abutoama, M.; Abdulhalim, I. Self-referenced biosensor based on thin dielectric grating combined with thin metal film. *Opt. Express* **2015**, *23*, 28667–28682. [CrossRef]
17. Lin, S.-F.; Wang, C.-M.; Ding, T.-J.; Tsai, Y.-L.; Yang, T.-H.; Chen, W.-Y.; Chang, J.-Y. Sensitive metal layer assisted guided mode resonance biosensor with a spectrum inversed response and strong asymmetric resonance field distribution. *Opt. Express* **2012**, *20*, 14584–14595. [CrossRef] [PubMed]
18. Lu, H.; Huang, M.; Kang, X.; Liu, W.; Dong, C.; Zhang, J.; Xia, S.; Zhang, X. Improving the sensitivity of compound waveguide grating biosensor via modulated wavevector. *Appl. Phys. Express* **2018**, *11*, 082202. [CrossRef]

19. Tu, Y.-K.; Tsai, M.-Z.; Lee, I.-C.; Hsu, H.-Y.; Huang, C.-S. Integration of a guided-mode resonance filter with microposts for in-cell protein detection. *Analyst* **2016**, *141*, 4189–4195. [CrossRef] [PubMed]
20. Ku, Y.F.; Li, H.Y.; Hsieh, W.H.; Chau, L.K.; Chang, G.E. Enhanced sensitivity in injection-molded guided-mode-resonance sensors via low-index cavity layers. *Opt. Express* **2015**, *23*, 14850–14859. [CrossRef]
21. Huang, Q.; Peh, J.; Hergenrother, P.J.; Cunningham, B.T. Porous photonic crystal external cavity laser biosensor. *Appl. Phys. Lett.* **2016**, *109*, 071103. [CrossRef] [PubMed]
22. Magnusson, R.; Wawro, D.; Zimmerman, S.; Ding, Y. Resonant Photonic Biosensors with Polarization-Based Multiparametric Discrimination in Each Channel. *Sensors* **2011**, *11*, 1476–1488. [CrossRef]
23. Zhang, M.; Lu, M.; Ge, C.; Cunningham, B.T. Plasmonic external cavity laser refractometric sensor. *Opt. Express* **2014**, *22*, 20347–20357. [CrossRef] [PubMed]
24. Wan, Y.; Krueger, N.A.; Ocier, C.R.; Su, P.; Braun, P.V.; Cunningham, B.T. Resonant Mode Engineering of Photonic Crystal Sensors Clad with Ultralow Refractive Index Porous Silicon Dioxide. *Adv. Opt. Mater.* **2017**, *5*, 1700605. [CrossRef]
25. Wang, L.; Sang, T.; Gao, J.; Yin, X.; Qi, H. High-performance sensor achieved by hybrid guide-mode resonance/surface plasmon resonance platform. *Appl. Opt.* **2018**, *57*, 7338–7343. [CrossRef]
26. Lan, G.; Zhang, S.; Zhu, Y.; Qing, L.; Li, D.; Nong, J.; Wang, W.; Chen, L.; Wei, W. High-performance refractive index sensor based on guided-mode resonance in all-dielectric nano-silt array. *Phys. Lett. A* **2019**, *383*, 1478–1482. [CrossRef]
27. Wang, Y.; Wu, T.; Kanamori, Y.; Hane, K. Freestanding HfO_2 grating fabricated by fast atom beam etching. *Nanoscale Res. Lett.* **2011**, *6*, 367. [CrossRef]
28. Quaranta, G.; Basset, G.; Martin, O.J.F.; Gallinet, B. Recent Advances in Resonant Waveguide Gratings. *Laser Photonics Rev.* **2018**, *12*, 1800017. [CrossRef]
29. Qian, L.; Wang, K.; Zhu, W.; Han, C.; Yan, C. Enhanced sensing ability in a single-layer guided-mode resonant optical biosensor with deep grating. *Opt. Commun.* **2019**, *452*, 273–280. [CrossRef]
30. Kerman, S.; Vercruysse, D.; Claes, T.; Stassen, A.; Hasan, M.U.; Neutens, P.; Mukund, V.; Verellen, N.; Rottenberg, X.; Lagae, L.; et al. Integrated Nanophotonic Excitation and Detection of Fluorescent Microparticles. *ACS Photonics* **2017**, *4*, 1937–1944. [CrossRef]
31. Kumar, S.; Park, H.; Cho, H.; Siddique, R.H.; Narasimhan, V.; Yang, D.; Choo, H. Overcoming evanescent field decay using 3D-tapered nanocavities for on-chip targeted molecular analysis. *Nat. Commun.* **2020**, *11*, 2930. [CrossRef] [PubMed]
32. Liu, W.; Li, Y.; Jiang, H.; Lai, Z.; Chen, H. Controlling the spectral width in compound waveguide grating structures. *Opt. Lett.* **2013**, *38*, 163–165. [CrossRef] [PubMed]
33. Moharam, M.G.; Gaylord, T.K. Rigorous coupled-wave analysis of planar-grating diffraction. *J. Opt. Soc. Am.* **1981**, *71*, 811–818. [CrossRef]
34. Lin, S.F.; Wang, C.M.; Tsai, Y.L.; Ding, T.J.; Yang, T.-H.; Chen, W.Y.; Yeh, S.F.; Chang, J.Y. A model for fast predicting and optimizing the sensitivity of surface-relief guided mode resonance sensors. *Sens. Actuators B Chem.* **2013**, *176*, 1197–1203. [CrossRef]
35. Tsai, M.-Z.; Hsiung, C.-T.; Chen, Y.; Huang, C.-S.; Hsu, H.-Y.; Hsieh, P.-Y. Real-time CRP detection from whole blood using micropost-embedded microfluidic chip incorporated with label-free biosensor. *Analyst* **2018**, *143*, 503–510. [CrossRef]
36. Sancho-Fornes, G.; Avella-Oliver, M.; Carrascosa, J.; Fernandez, E.; Brun, E.M.; Maquieira, Á. Disk-based one-dimensional photonic crystal slabs for label-free immunosensing. *Biosens. Bioelectron.* **2019**, *126*, 315–323. [CrossRef] [PubMed]
37. Lu, X.; Wan, R.; Zhang, T. Metal-dielectric-metal based narrow band absorber for sensing applications. *Opt. Express* **2015**, *23*, 29842–29847. [CrossRef]